With $\dot{n}_{mo}$ being -25.1 ± 1.3 arcsec per century^2 in La90, and the relationships that 1 arcsec per century$^2 = 4.868 \times 10^{-25}$ rad s^{-2}, the present-day $\dot{\Omega}_{tidal}$ value is equivalent to a ΔLOD of $+2.3 \pm 0.2$ ms per century.

Received 6 April; accepted 11 December 2000.

1. Laskar, J. The chaotic motion of the solar system: A numerical estimate of the size of the chaotic zones. *Icarus* **88,** 266–291 (1990).
2. Laskar, J. The limits of Earth orbital calculations for geological time scale use. *Phil. Trans. R. Soc. Lond. A* **357** 1735–1759 (1999).
3. Laskar, J., Joutel, F. & Boudin, F. Orbital precessional, and insolation quantities for the Earth from −20 to +10 Myr. *Astron. Astrophys.* **270,** 522–533 (1993).
4. Quinn, T. R., Tremaine, S. & Duncan, M. A. A three million year integration of the Earth's orbit. *Astron. Journal* **101,** 2287–2305 (1991).
5. Dehant, V., Loutre, M.-F. & Berger, A. Potential impact of the Northern Hemisphere Quaternary ice sheets on the frequencies of the astroclimatic orbital parameters. *J. Geophys. Res.* **95,** 7573–7578 (1990).
6. Tushingham, A. M. & Peltier, W. R. ICE-3G: A new global model of late Pleistocene deglaciation based on geophysical predictions of post-glacial relative sea level change. *J. Geophys. Res.* **96,** 4497–4523 (1991).
7. Peltier, W. R. & Jiang, X. The precession constant of the Earth: Variations through the ice age. *Geophys. Res. Lett.* **21,** 2299–2302 (1994).
8. Mitrovica, J. X. & Forte, A. M. Pleistocene glaciation and the Earth's precession constant. *Geophys. J. Int.* **121,** 21–32 (1995).
9. Mitrovica, J. X. & Forte, A. M. Radial profile of mantle viscosity: Results from the joint inversions of convection and postglacial rebound observables. *J. Geophys. Res.* **102(B2),** 2751–2769 (1997).
10. Mitrovica, J. X., Forte, A. M. & Pan, R. Glaciation-induced variations in the Earth's precession frequency, obliquity and insolation over the last 2.6 Ma. *Geophys. J. Int.* **128,** 270–284 (1997).
11. Forte, A. M. & Mitrovica, J. X. A resonance in the Earth's obliquity and precession over the past 20 Myr driven by mantle convection. *Nature* **390,** 676–679 (1997).
12. Stephenson, F. R. & Morrison, L. V. Long-term fluctuations in the Earth's rotation: 700 BC to AD 1990. *Phil. Trans. R. Soc. Lond. A* **351,** 165–202 (1995).
13. Lourens, L. J. *et al.* Evaluation of the Plio-Pleistocene astronomical timescale. *Paleoceanography* **11,** 391–413 (1996).
14. Wehausen, R. & Brumsack, H.-J. Chemical cycles in Pliocene sapropel-bearing and sapropel-barren eastern Mediterranean sediments. *Palaeogeogr. Palaeoclimatol. Palaeoecol.* **158,** 325–352 (2000).
15. Kroon, D. *et al.* Oxygen isotope and sapropel stratigraphy in the eastern Mediterranean during the last 3.2 million years. *Proc. ODP Sci. Res.* **160,** 181–189 (1998).
16. Hilgen, F. J. Astronomical calibration of Gauss to Matuyama sapropels in the Mediterranean and implications for the geomagnetic polarity time scale. *Earth Planet. Sci. Lett.* **104,** 226–244 (1991).
17. Venkatarathnam, K. & Ryan, B. F. Dispersal patterns of clay minerals in the eastern Mediterranean Sea. *Mar. Geol.* **11,** 261–282 (1971).
18. Rossignol-Strick, M. African monsoons: an immediate climate response to orbital insolation. *Nature* **304,** 46–49 (1983).
19. Raymo, M. E., Ruddiman, W. F., Backman, J., Clement, B. M. & Martinson, D. G. Late Pliocene variation in northern hemisphere ice sheets and North Atlantic Deep Water circulation. *Paleoceanography* **4,** 413–446 (1989).
20. Lambeck, K. *The Earth's Variable Rotation: Geophysical Causes and Consequences* (Cambridge University Press, Cambridge, 1980).
21. Clemens, S. C., Murray, D. W. & Prell, W. L. Nonstationary phase of the Plio-Pleistocene Asian monsoon. *Science* **274,** 943–948 (1996).
22. Imbrie, J. *et al.* in *Milankovitch and Climate* (eds Berger, A., Imbrie, J., Hays, J., Kukla, G. & Satzman, B.) 269–305 (Reidel, Dordrecht, 1984).
23. Bard, E., Hamelin, B. & Fairbanks, R. G. U-Th ages obtained by mass spectrometry in corals from Barbados: sea level during the last 1300,000 years. *Nature* **345,** 405–410 (1990).
24. Lawrence-Edwards, R., Chen, J. H., Ku, T.-L. & Wasserburg, G. J. Precise timing of the last interglacial period from mass-spectrometric determination of thorium-230 in corals. *Science* **236,** 1547–1553 (1987).
25. Sakamoto, T., Janecek, T. & Emeis, K.-C. Continuous sedimentary sequences from the eastern Mediterranean sea: Composite depth sections. *Proc. ODP Sci. Res.* **160,** 37–59 (1998).
26. Gordeyev, V. V. & Lisitsyn, A. P. The average chemical composition of suspensions in the world's rivers and the supply of sediments to the ocean by streams. *Dokl. Earth Sci.* **238,** 150–153 (1978). (Transl.)
27. Martin, J.-M. & Meybeck, M. elemental mass-balance of material carried by major world rivers. *Mar. Chem.* **7,** 173–206 (1979).
28. Ganor, E. & Mamane, Y. Transport of Saharan dust across the eastern Mediterranean. *Atmos. Environ.* **16,** 581–587 (1982).
29. Ganor, E., Foner, H. A., Brenner, S., Neeman, E. & Lavi, N. The chemical composition of aerosols settling in Israel following dust storms. *Atmos. Environ. A* **25,** 2665–2670 (1991).
30. Paillard, D., Labeyrie, L. & Yiou, P. AnalySeries 1.1—Macintosh program performs time-series analysis. *Eos* **77,** 379 (1996).

Acknowledgements

We thank F. J. Hilgen, J. Laskar, J. X. Mitrovica, G. J. Reichart, J. Steenbrink and J. W. Zachariasse for discussions and comments, and J. Laskar and J. X. Mitrovica in particular for providing the astronomical solution and Earth model calculations, respectively. This work was supported by the Dutch National Science Foundation (NWO) and the German Science foundation (DFG) through ODP-SPP.

Correspondence and requests for materials should be addressed to L.J.L. (e-mail: llourens@geo.uu.nl).

Cranial design and function in a large theropod dinosaur

Emily J. Rayfield*, David B. Norman*†, Celeste C. Horner‡, John R. Horner‡, Paula May Smith*, Jeffrey J. Thomason§ & Paul Upchurch*

** Department of Earth Sciences, University of Cambridge, Downing Street, Cambridge CB2 3EQ, UK*
‡ Museum of the Rockies, Montana State University, Bozeman, Montana, 59717, USA
§ Department of Biomedical Sciences, Ontario Veterinary College, University of Guelph, Guelph, Ontario, Canada, N1G 2W1
† Present address: Department of Paleobiology, National Museum of Natural History, Smithsonian Institution, Washington DC 20560, USA

Finite element analysis (FEA)[1] is used by industrial designers and biomechanicists to estimate the performance of engineered structures or human skeletal and soft tissues subjected to varying regimes of stress and strain[2–4]. FEA is rarely applied to problems of biomechanical design in animals, despite its potential to inform structure–function analysis. Non-invasive techniques such as computed tomography scans can be used to generate accurate three-dimensional images of structures, such as skulls, which can form the basis of an accurate finite element model. Here we have applied this technique to the long skull of the large carnivorous theropod dinosaur *Allosaurus fragilis*[5]. We have generated the most geometrically complete and complex FEA model of the skull of any extinct or extant organism and used this to test its mechanical properties and examine, in a quantitative way, long-held hypotheses concerning overall shape and function[6–8]. The combination of a weak muscle-driven bite force, a very 'light' and 'open' skull architecture and unusually high cranial strength, suggests a very specific feeding behaviour for this animal. These results demonstrate simply the inherent potential of FEA for testing mechanical behaviour in fossils in ways that, until now, have been impossible.

A 3D finite element model of the complete skull of the top Late Jurassic predator[9–11] *Allosaurus fragilis* has been generated (Fig. 1a–c), using data from serial computed tomography (CT) scan images. This model has been loaded in order to simulate four different

Table 1 Bite force estimates for some living and extinct vertebrates

Species	Bite force	Calculation
Allosaurus fragilis biting mode A	805.42 N total	Low estimate bilateral static bite* at maxillary teeth 3, 4 and 5
Allosaurus fragilis biting mode B	2,147.88 N total	High estimate bilateral static bite at maxillary teeth 3, 4 and 5
Allosaurus fragilis biting mode C	18,746.76 N total	Maximum bilateral force at maxillary teeth 3, 4 and 5; with muscular and condylar force*
Allosaurus fragiis biting mode D	55,446.96 N total	Maximum bilateral force at maxillary teeth 3, 4 and 5; without musuclar and condylar force*
Allosaurus fragilis	3,572.56 N	High estimate bilateral force at most posterior maxillary tooth 16
Tyrannosaurus rex	13,400 N†	Single tooth, possible unilateral bite, tooth impact velocity and adhering flesh accounted for
Alligator missippiensis	13,000†	Unknown
Panthera leo (lion)	4,167.60 N‡	Calculated bilateral bite at molars
Panthera pardus (leopard)	2,268.7 N‡	Calculated bilateral bite at molars
Felis concolor (cougar)	1,836.8 N‡	Calculated bilateral bite at molars
Canis lupus (wolf)	1,412.2 N‡	Calculated bilateral bite at molars
Vulpes vulpes (red fox)	532.4 N‡	Calculated bilateral bite at molars

* Maximum tensile/compressive stress 200 MPa.
† Taken from ref. 12.
‡ Taken from ref. 28.

modes of biting (Loading conditions A to D; see Methods and Table 1). Biting modes A and B simulate a static bite generated only by the adductor (jaw closing) muscles (Fig. 1d). It is assumed that the skull is in equilibrium, with the jaws closing against a prey item. Dorsally directed bite forces were applied to the large maxillary teeth (nos 3–5, Fig. 1d) midway along the upper jaw. Corresponding forces were applied at the jaw joint (Fig. 1d) and at the origination sites of the principal jaw closing muscles (Fig. 1d, black arrowheads). Although not specifically a life situation, it was assumed that all adductor muscles were contracting maximally at the time of the bite to assess the maximum values of cranial stress.

For mode A, the applied bite force represents a minimum estimate based on an ectothermic model of dinosaur physiology (see Methods for calculation). Forces in mode B represent a maximum estimate, using a homeothermic (endothermic) model (Table 1). The true bite force, condylar force and peak stresses experienced during a muscle-driven bite lie somewhere within the range of values calculated for modes A and B, exact values being a subjective matter based on personal views of dinosaur physiology.

In an attempt to estimate the strength of the skull, modes C and D represent the maximum forces that could be applied to the same impact teeth as in modes A and B before the cranium began to yield. To obtain these values, force magnitudes were increased iteratively until peak stresses reached yield point. In mode C the jaw adductors were considered to have been maximally active, and therefore tensioning the skull (Fig. 1d), whereas in mode D, the musculature was quiescent, so that the skull frame reacts passively to externally applied forces (parameters as in Fig. 1d, but without muscle and

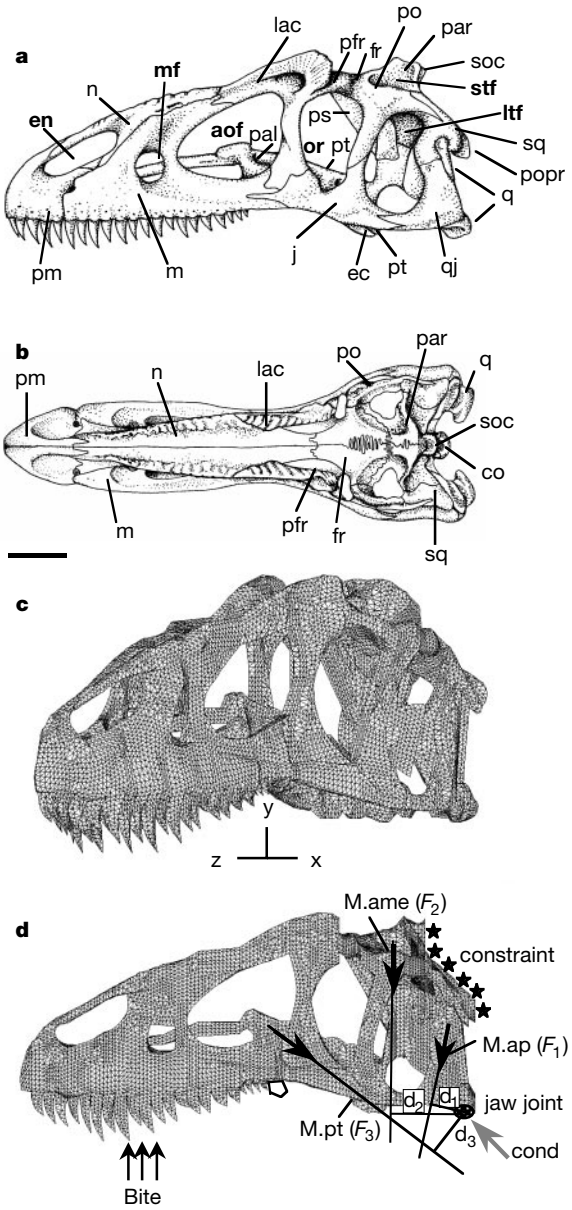

Figure 1 The skull of *Allosaurus fragilis*. **a**, Lateral view. **b**, Dorsal view. aof, antorbital fenestra; co, occipital condyle; ec, ectopterygoid; en, external naris; fr, frontal; j, jugal; lac, lacrimal; ltf, lower temporal fenestra; m, maxilla; mf, maxillary fenestra; n, nasal; or, orbit; pal, palatine; par, parietal; pfr, prefrontal; pm, premaxilla; po, postorbital; popr, paraoccipital process; ps, parasphenoid; pt, pterygoid; q, quadrate; qj, quadratojugal; soc, supraoccipital; sq, squamosal; stf, supratemporal fenestra. Scale bar, 10 cm. **c**, Meshed finite element model of *Allosaurus fragilis* in oblique view. **d**, Meshed finite element model in lateral view. Black stars, position of constraint; thick black arrows, line and direction of muscular force; thinner black arrows and 'bite', point of bite force; grey arrow, line and direction of condylar force; cond, point of condylar force; M.ap (F_1), M. adductor posterior; M.ame (F_2), M. adductor mandibulae externus superficialis, medius, profundus and M. pseudotemporalis; M.pt (F_3), M. pterygoideus group; d_1, moment arm of muscle F_1; d_2, moment arm of muscle F_2; d_3, moment arm of muscle F_3.

condylar force application). All models were anchored at the occipital surface on the rear of the skull (Fig. 1d, black stars), mimicking the stabilizing action of the vertebral column, cervical and axial musculature, and assuming that neck musculature was holding the head rigid rather than imparting any retractile forces.

Patterns of cranial stress distribution are similar for the four loading conditions. Stress magnitudes vary predictably, with higher magnitudes found where higher bite and jaw joint forces have been applied. The results of our analyses offer a number of hitherto unappreciated insights into the way the *Allosaurus* skull was designed functionally to resist bite- and impact-induced stresses in life.

First, compared with values for extant mammalian taxa, the muscle-driven bite force of *Allosaurus fragilis* appears to be relatively weak (Table 1). Also, *Allosaurus* adductor-generated bites are in no way comparable to estimated *Alligator missippiensis* and *Tyrannosaurus rex* bite forces, both in the region of 13,000 N (ref. 12).

Second, in contrast to these weak muscular-driven bite forces, the skull is strong enough to withstand extremely large maximum forces at the tooth row before yielding because of tensional stress (Table 1, modes C and D; Fig. 2a, b). Although bone is much weaker in shear when tested mechanically, peak shear stresses in the skull are an order of magnitude lower than principal tension and compression. Should the dentition dislodge before skull failure, this would serve only to protect the skull from peak stresses making it more resilient. When all adductor musculature is contracting maximally and a condylar force is applied (mode C), the skull can withstand between 8.7 and 23.3 times the estimated muscle-driven bite force before yielding (Table 1, Fig. 2a, b). When the tensioning effect of muscular forces and the compressional effect of condylar forces are removed from the model (that is, mode D), the maximum force withstood by the tooth row may be up to 69 times the estimated muscle-driven bite force (Fig. 2b). Such strength of the skull means forces in the region of 55,000 N may be withstood by the skull (Fig. 2a, b). It appears that the skull is designed to be extremely strong when biting at the central maxillary teeth.

Third, tensile stresses ventrally and compressive ones dorsally reflect the bending moments acting on the skull during loading (Fig. 3a, b). However, the skull of *Allosaurus* seems to be designed to resist large vertically directed forces applied along the tooth row. In all biting modes, compressive stresses not absorbed by the robust ventral maxilla (Fig. 1a, m) trace vector arcs from the impact teeth through the nasals and through the lateral struts forming the sidewall of the skull (Fig. 3b–d). Some vectors approach the skull roof, composed of thick, centrally located parietals and frontals (Fig. 1b, par, fr; Fig. 3d) that absorb a certain amount of stress. Many compressive vectors are routed in loops around the large cranial fenestrae (window-like openings in the skull) (Fig. 3b, c, d); these 'functional loops' minimize stress and strain in response to applied forces[13]. Such fenestrae (Fig. 1a, aof) appear to be important in stress management in the skull, and non-mechanical interpretations of the antorbital fenestra as a cavity housing a gland or air sac diverticulum[14] appear to be of lesser importance.

Studies suggest that the large Cretaceous carnivore *T. rex*, with stout, conical teeth and an extremely robust skull[15], could withstand tooth–bone impacts during feeding, and was capable of generating jaw-closure forces large enough to shatter skeletal material during prey dismemberment[12,16,17]. A weak muscle-driven bite indicates that *Allosaurus* was not capable of splintering bony food material in this manner. In contrast to *T. rex*, *Allosaurus* displays recurved, laterally compressed teeth adapted for slashing or slicing[8] and a more lightly constructed but extremely strong skull (Fig. 1a, b)[5]. We believe that this 'weak bite/strong skull' functional paradox may be explained by the predatory behaviour of *Allosaurus*.

Part of the overall high strength estimate for the allosaur skull can be accounted for by considering built-in safety factors; the ratio of a structure's capacity or strength, compared with the highest expected load the structure experiences during everyday use[18]. Mammalian cranial bone may operate at a safety factor of between 1.8 and 11(ref. 19). However, the very large difference between muscle-driven bite forces and the maximum force that can be applied to the skull before yielding (Fig. 2a, b) suggests that the *Allosaurus* cranium is overengineered. If the animal was to experience large forces such as those created by a high velocity impact of skull into prey, as part of its regular feeding strategy, the skull could still function within acceptable bounds of safety and the apparent overcompensation of design can be explained.

Our results provide quantitative evidence to suggest that during attack or feeding, *Allosaurus* generally used a high velocity impact of the skull into its prey; an analogue would be a person wielding a large, heavy hatchet. Aided by sharp, recurved teeth and powerful neck musculature driving the skull downwards and then imparting a retractile force, portions of flesh were sliced, torn away and

a

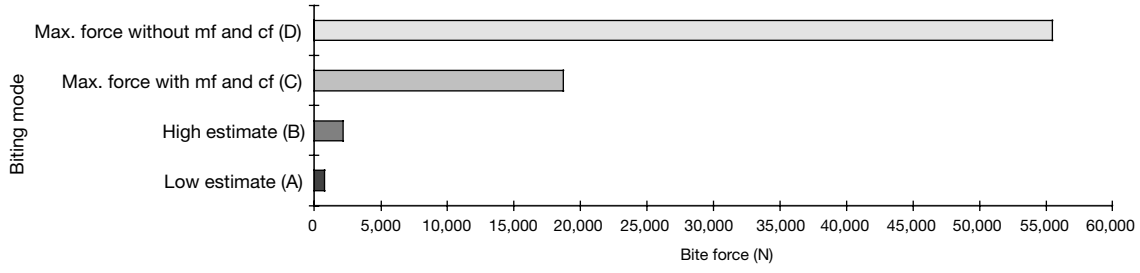

b

Bite position	Range of adductor-generated bite force. mode A and B	Maximum bite force with muscle and condylar force applied. mode C	Ratio of adductor force: maximum force*	Maximum bite force without muscle and condylar force. mode D	Ratio of adductor force: maximum force†
Central	805 to 2,148 N	18,747 N	23.3 to 8.7	55,447 N	68.8 to 25.8

* Where maximum force = maximum bite force when muscular and condylar forces are applied
† Where maximum force = maximum bite force when muscular and condylar forces are not applied

Figure 2 Estimated bite forces and skull strength. **a**, Difference between muscular-generated bite force, modes A and B; and maximum force before yielding, modes C and D. cf, condylar force; mf, muscle force. **b**, Table depicting ratios between muscular generated bite force and maximum force in modes C and D respectively.

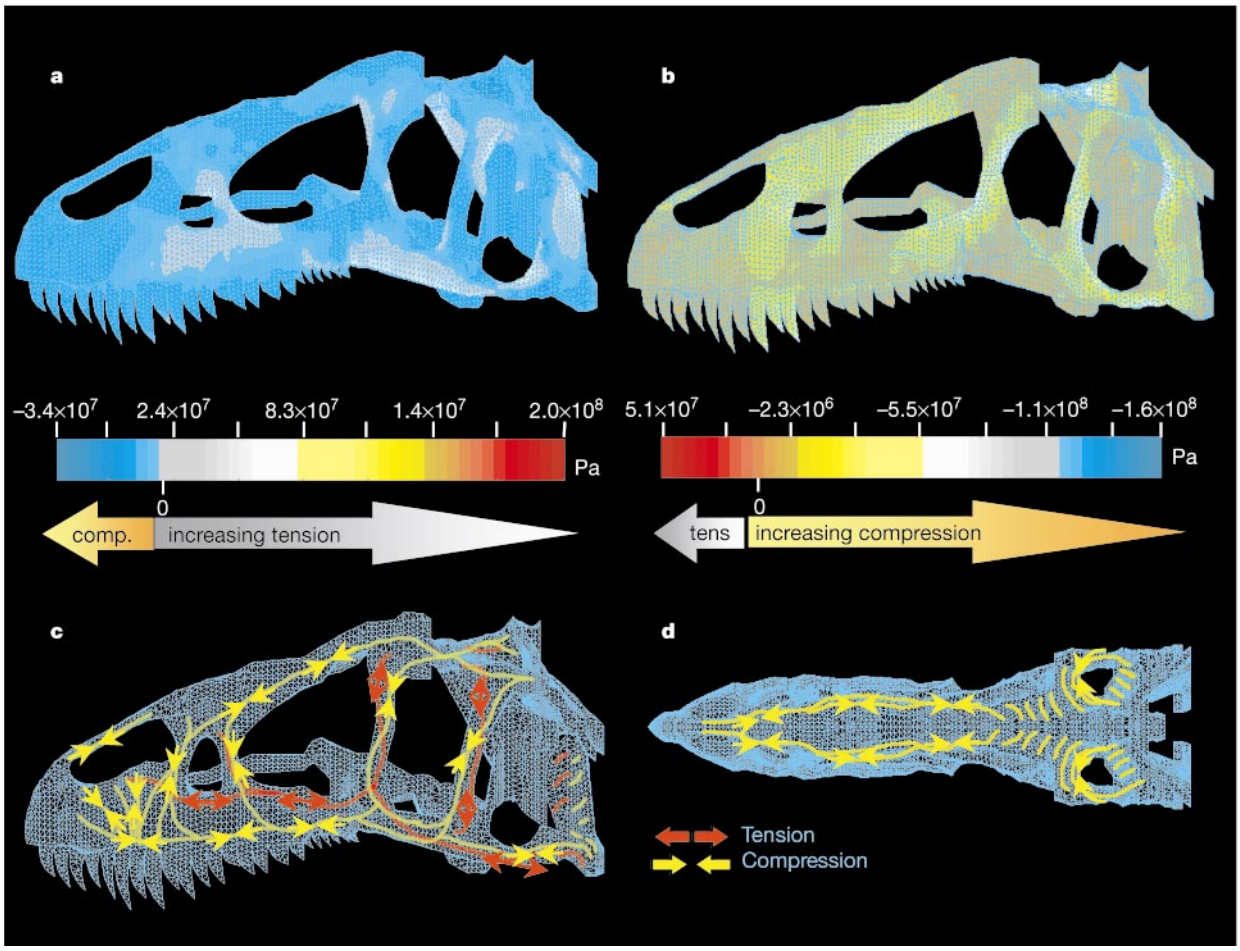

Figure 3 Stress distribution and vector plots for the skull of *Allosaurus fragilis* during a maximum impact bite without adductor muscle contraction (mode D). **a**, Stress distribution and magnitude plot for principal stress 1, lateral view. Colour scale bar indicates areas of high tension or compression. **b**, Stress distribution and magnitude plot for principal stress 3, lateral view. See colour scale bar for areas of high tension or compression. **c**, Stylized plot showing stress vector direction, lateral view. **d**, Stylized stress vector plot, dorsal view.

swallowed (a strategy similar to that seen in *Varanus komodoensis*[20]). The crushing bite of *T. rex* represents a specialization towards carcass dismemberment and possibly tackling larger, heavily armoured prey. By contrast, *Allosaurus* may have 'traded' a heavy skull and bite strength for greater speed and mobility of upper jaw impact in order to capture lighter and more agile forms such as ornithopod dinosaurs[21]. *Allosaurus* might have ambushed larger, more dangerous, prey (for example, stegosaurs and sauropods) by inflicting a sudden devastating high-impact attack bite before the defender could retaliate.

The skull of *Allosaurus fragilis* is designed to allow this dinosaur to adopt a high impact 'slash and tear' mode of prey attack and feeding, rather than relying on a devastatingly powerful muscle-driven bite. The high cranial stresses associated with this mode of feeding are accommodated primarily by using a 'functional loop' model; this explains the unusually light and fenestrate architecture of the skull in an animal of this size. This analysis illustrates how, used with appropriate caution, FEA can be an important tool in analyses of mechanical behaviour in fossils. □

Methods

Skull mapping

An almost complete skull of *Allosaurus fragilis* from the Museum of the Rockies (MOR 693) was subjected to CT to obtain a series of transaxial scan images separated by 4-mm intervals. *x,y* coordinates from the CT images were imported into the finite element modelling and analysis package COSMOS/M (version 2.0, Structural Research and Analysis Corp., CA, USA). Coordinates were used as a framework for the 3D geometry of *Allosaurus*. Resolution of CT scans was such that internal features, such as pneumatic cavities, could be identified and incorporated into the geometry of the model. The model was meshed creating solid four-noded tetrahedral elements (Fig. 1c). Number of elements = 146,398; nodes = 38,344; degrees of freedom = 107,421. Because the coordinates were calibrated initially, the model was to scale.

Material properties

Histologically, the bone of theropods most closely resembles the bone of fast-growing bovine mammals[22]. Studies of *Allosaurus* cranial bone[22] have shown it to be composed of secondary remodelled haversian bone with primary compact bone restricted to the surface[22]. Assuming that similar bone histology indicates broadly similar material properties, and to avoid overestimating maximum tension and compression, this model was assigned the material properties of bovine haversian bone: Young's modulus = 10 GPa; shear modulus = 3.6 GPa; poisson ratio = 0.4; density = 1.895 (ref. 23). The omission of compact bone from our model may lead to an underestimation of strength of the skull. However, inclusion of such strengthening characteristics would only serve to increase strength of the skull and provide further support for our conclusions concerning the difference between adductor-generated bite force and maximum force at failure. Properties of bovine dentine were applied to the teeth: Young's modulus = 21 GPa; shear modulus = 8 GPa; poisson ratio = 0.31; density = 2.076 (ref. 24).

Soft tissues

Adductor muscles were reconstructed in clay around a life-size cast of *Allosaurus*, and then incised at their widest part and the cross-sectional surface area measured. Cross-sectional areas were recorded digitally in Scion Image for Windows 95, 98 and NT, Beta 3b Version, an image analysis program for PC based on NIH image for Macintosh (http://www.scioncorp.com/index.htm). Adductor muscle force was calculated from muscle

stress values known from extant vertebrates. As these values range from 147 to 392 kPa (ref. 25), a low (mode A) and a high (mode B) estimate of possible muscle force were calculated using the extremes of this range. As stated in the text, the true muscle force values of *Allosaurus* lie within this range—exactly where depends on the animal's physiology. Ventrally directed muscle forces were applied at the attachment sites of all adductor muscles in the correct line of action based upon the anatomy of the lower jaw. Adductor muscles were grouped into three functional units. F_1 = M. adductor posterior; F_2 = M. adductor mandibulae externus group (comprising MAME superficialis, medialis and profundus) and M. pseudotemporalis; F_3 = M. pterygoideus anterior and posterior. The angles between lines of muscle action and the vertical were measured: for F_1, $\alpha = 11°$; for F_2, $\beta = 3°$; for F_3, $\gamma = 62°$.

Bite force calculation

To calculate a static, muscle-driven bite, it is assumed that all muscles are acting in a single parasagittal plane and that the skull is in equilibrium. In these models, *Allosaurus* is biting bilaterally at six teeth in total, the 3rd, 4th and 5th maxillary teeth, left and right sides (see Fig. 1d for details). Thus, three independent equations containing four unknowns are derived. One further assumption must be made; in this case that bite force is vertical. Equations calculate force on one side of the skull only, as forces are equal on both sides. The following equations are used (after refs 26, 27).

$$P\cos\theta + 3B = F_1\cos\alpha + F_2\cos\beta + F_3\cos\gamma \quad (1)$$

$$P\sin\theta + F_1\sin\alpha + F_2\sin\beta = F_3\sin\gamma \quad (2)$$

$$B[\chi_1 + (\chi_1 + \chi_2) + (\chi_1 + \chi_2 + \chi_3)] = F_3 d_3 + F_2 d_2 + F_1 d_1 \quad (3)$$

Where P = condylar force, θ = angle of condylar force, $3B$ = total bite force at three adjacent teeth ($3B/3$ = bite force per tooth). F_1, F_2 and F_3 = adductor muscle force values (low estimate: F_1 = 228.88 N; F_2 = 1173.86 N; F_3 = 1,350.486 N, high estimate: F_1 = 610.3 N; F_2 = 3,130.51 N; F_3 = 3,601.32 N). α, β, γ = angles from vertical for adductor muscle forces (as above). χ_1 = distance from jaw joint to max. 5; χ_2 = distance from max. 5 to max. 4; χ_3 = distance from max. 4 to max. 3; d_1 to d_3 = moment arms for muscle groups F_1 to F_3, respectively; d_1 = 0.0925 m; d_2 = 0.132 m; d_3 = 0.066 m.

Using a high and a low estimate of muscle force leads to a high and a low estimate of bite force and condylar force (Table 1). Again, 'true' values lie within this range. By calculating such a range, assumptions concerning validity of loading parameters may be limited. Low estimate condylar force = 1,957.90 N per condyle; high estimate condylar force = 5,221.46 N per condyle. Angle of condylar forces from the vertical = 33.73°. Comparison with previously published bite force equations[26,27] suggests that experimental error in the calculation of *Allosaurus* bite force is unlikely.

Finite element analysis calculates reaction to the applied load and a defined constraint for each element in turn, to give a composite picture of the mechanical behaviour of the skull (see Fig. 3).

For full descriptions of bite forces for all models featured in this analysis, see Table 1.

Received 24 March; accepted 22 November 2000.

1. Zienkiewicz, O. C. in *The Finite Element Method in Engineering Science* 521 (McGraw-Hill, London, 1971).
2. Ross, C. T. F. in *Finite Element Methods in Engineering Science* 519 (Ellis Horwood, London, 1990).
3. Huiskes, R. & Chao, E. Y. S. A survey of finite element analysis in orthopedic biomechanics: The first decade. *J. Biomechanics* **16,** 385–409 (1983).
4. Huiskes, R. & Hollister, S. J. From structure to process, From organ to cell: Recent developments of FE-analysis in orthopaedic biomechanics. *J. Biomech. Eng., Trans. ASME* **115,** 520–527 (1993).
5. Madsen, J. H. Jr *Allosaurus fragilis*: A Revised Osteology. *Utah Geol. Min. Surv. Bull.* **109,** 1–163 (1976).
6. Paul, G. S. in *Predatory Dinosaurs of The World* 464 (Simon and Schuster, New York, 1988).
7. Farlow, J. O. Speculations about the diet and foraging behaviour of large carnivorous dinosaurs. *Am. Mid. Nat.* **95,** 186-191 (1976a).
8. Farlow, J. O., Brinkman, D. L., Abler, W. L. & Currie, P. J. Size, shape, and serration density of theropod dinosaur lateral teeth. *Mod. Geol.* **16,** 161–198 (1991).
9. Dodson, P., Behrensmeyer, A. K., Bakker, R. T. & McIntosh, J. S. Taphonomy and paleoecology of the dinosaur beds of the Jurassic Morrison Formation. *Paleobiol.* **6,** 208–232 (1980).
10. Molnar, R. E. & Farlow, J. O. in *The Dinosauria* (eds Weishampel, D. B., Dodson, P. & Osmolska, H.) 210–224 (Univ. California Press, Berkeley, 1990).
11. Perez-Moreno, B. P. *et al.* On the presence of *Allosaurus fragilis* (Theropoda: Carnosauria) in the Upper Jurassic of Portugal: first evidence of an intercontinental dinosaur species. *J. Geol. Soc. Lond.* **156,** 449–452 (1999).
12. Erickson, G. M. *et al.* Bite-force estimation for *Tyrannosaurus rex* from tooth-marked bones. *Nature* **382,** 706–708 (1996).
13. Buckland-Wright, J. C. Bone structure and the patterns of force transmission in the cat skull (*Felis catus*). *J. Morph.* **155,** 35–62 (1978).
14. Witmer, L. M. The Evolution of the Antorbital Cavity of Archosaurs: A study in soft-tissue reconstruction in the fossil record with an analysis of the function of pneumaticity. *J. Vert. Paleo. Mem.* **17,** 1–73 (1997).
15. Molnar, R. E. The cranial morphology of *Tyrannosaurus rex. Palaeontographica Abr. A.* **217,** 137–176 (1991).
16. Chin, K., Tokaryk, T. T., Erickson, G. M. & Calk, L. C. A king-sized theropod coprolite. *Nature* **393,** 680–682 (1998).
17. Erickson, G. M. & Olson, K. H. Bite marks attributable to *Tyrannosaurus rex*: preliminary description and implications. *J. Vert. Paleontol.* **16,** 175–178 (1996).
18. Diamond, J. M. in *Principles of Animal Design: The Optimization and Symmorphosis Debate* (eds Weibel, E. R., Taylor, C. R. & Bolis, L.) 21–27 (Cambridge Univ. Press, Cambridge, 1998).
19. Thomason, J. J. & Russell, A. P. Mechanical factors in the evolution of the mammalian secondary palate: a theoretical analysis. *J. Morph.* **189,** 199–213 (1986).
20. Auffenberg, W. *The Behavioural Ecology of the Komodo Monitor.* (Univ. Florida Press, Gainesville, Florida, 1981).
21. Sues, H. D. & Norman, D. B. in *The Dinosauria* (eds Weishampel, D. B., Dodson, P. & Osmolska, H.) 498–509 (Univ. California Press, Berkeley, 1990).
22. Reid, R. E. H. Bone histology of the Cleveland-Lloyd dinosaurs and of dinosaurs in general. *Brig. Young Univ. Geol. Stud.* **41,** 25–71 (1996).
23. Reilly, D. T. & Burstein, A. H. The elastic and ultimate properties of compact bone tissue. *J. Biomech.* **8,** 393–405 (1975).
24. Waters, N. E. in *The Mechanical Properties of Biological Materials* (eds Vincent, J. F. V & Currey, J. D.) 99–135 (Cambridge Univ. Press, Cambridge, 1980).
25. Thomason, J. J., Russell, A. P. & Morgelli, M. Forces of biting, body size, and masticatory muscle tension in the opossum *Didelphis virginiana*. *Can. J. Zool.* **68,** 318–324 (1990).
26. Crompton, A. W. & Hylander, W. L. in *The Ecology and Biology of Mammal Like Reptiles* (eds Hotton, N., Maclean, P. D., Roth, J. J. & Roth, E. C.) 263–282 (Smithsonian Institution Press, Washington DC, 1986).
27. Sinclair, A. G. & Alexander, R. M. Estimated forces exerted by the jaw muscles of some reptiles. *J. Zool.* **213,** 107–115 (1987).
28. Thomason, J. J. Cranial strength in relation to estimated biting forces in some mammals. *Can. J. Zool.* **69,** 2326–2333 (1991).

Acknowledgements

We are grateful to the Bozeman Hospital, Montana, USA, and Picker CT scan Company for CT scanning and file conversion; R. E. H. Reid for advice on dinosaur bone histology and material properties; and M. Harwood for COSMOS/M technical support. J. R. Horner provided access to *Allosaurus fragilis* (MOR 693), C. C. Horner provided use of computing equipment and aided file conversion; P. May Smith assisted with bite force calculations; S. Evans provided crocodile and alligator material for dissection and R. Felix advised on coordinate capture and image production. This work was supported by The Royal Society (D.B.N.), the Natural Environment Research Council, The Department of Earth Sciences and Emmanuel College, Cambridge University and the Cambridge Philosophical Society, and the British Federation of Women Graduates (E.J.R.).

Correspondence and requests for material should be addressed to E.J.R. (email: eray@esc.cam.ac.uk).

Genetic evidence against panmixia in the European eel

Thierry Wirth & Louis Bernatchez

GIROQ, Département de Biologie, Université Laval, Ste-Foy, Québec G1K7P4, Canada

The panmixia hypothesis—that all European eel (*Anguilla anguilla*) migrate to the Sargasso Sea for reproduction and comprise a single, randomly mating population—is widely accepted[1,2]. If true, then this peculiar life history strategy would directly impact the population genetics of this species, and eels from European and north African rivers should belong to the same breeding population through the random dispersal of larvae. To date, the panmixia hypothesis has remained unchallenged: genetic studies realized on eel's mitochondrial DNA failed to detect any genetic structure[3–5]; and a similar lack of structure was found using allozymes[6,7], with the exception of clinal variation imposed by selection[8,9]. Here we have used highly polymorphic genetic markers that provide better resolution[10,11] to investigate genetic structure in European eel. Analysis of seven microsatellite loci among 13 samples from the north Atlantic, the Baltic Sea and the Mediterranean Sea basins reveals that there is global genetic differentiation[12]. Moreover, pairwise Cavalli-Sforza and Edwards'[13] chord distances correlate significantly with coastal geographical distance. This pattern of genetic structure implies